nature materials

ARTICLES

PUBLISHED ONLINE: 24 JULY 2017 | DOI: 10.1038/NMAT4953

A magnetic topological semimetal $Sr_{1-y}Mn_{1-z}Sb_2$ ($y, z < 0.1$)

J. Y. Liu[1†], J. Hu[1†], Q. Zhang[2,3†], D. Graf[4], H. B. Cao[3], S. M. A. Radmanesh[5], D. J. Adams[5], Y. L. Zhu[1], G. F. Cheng[1,6], X. Liu[1], W. A. Phelan[2], J. Wei[1], M. Jaime[7], F. Balakirev[7], D. A. Tennant[3], J. F. DiTusa[2], I. Chiorescu[4,8], L. Spinu[5] and Z. Q. Mao[1*]

Weyl semimetals (WSMs) evolve from Dirac semimetals in the presence of broken time-reversal symmetry (TRS) or space-inversion symmetry. The WSM phases in TaAs-class materials and photonic crystals are due to the loss of space-inversion symmetry. For TRS-breaking WSMs, despite numerous theoretical and experimental efforts, few examples have been reported. In this Article, we report a new type of magnetic semimetal $Sr_{1-y}Mn_{1-z}Sb_2$ ($y, z < 0.1$) with nearly massless relativistic fermion behaviour ($m^* = 0.04-0.05m_0$, where m_0 is the free-electron mass). This material exhibits a ferromagnetic order for $304\,K < T < 565\,K$, but a canted antiferromagnetic order with a ferromagnetic component for $T < 304\,K$. The combination of relativistic fermion behaviour and ferromagnetism in $Sr_{1-y}Mn_{1-z}Sb_2$ offers a rare opportunity to investigate the interplay between relativistic fermions and spontaneous TRS breaking.

Three-dimensional (3D) Dirac semimetals (DSMs) can be viewed as 3D analogues of graphene and are characterized by linear energy–momentum dispersions near the Fermi level along all three momentum directions[1–6]. The linear band crossing point, that is, the Dirac point, is protected against gap formation by crystal symmetry. Such unique band structures of 3D DSMs result in peculiar, exotic properties such as high bulk carrier mobility[7] and large linear magnetoresistance[7,8]. 3D DSMs have been experimentally realized in many material systems such as Na_3Bi (ref. 2), Cd_3As_2 (refs 4–6), $ZrTe_5$ (ref. 9) and so on. Moreover, a new form of DSM state featuring Dirac band crossing along a line/loop has also been established in $PbTaSe_2$ (ref. 10), $PtSn_4$ (ref. 11) and ZrSiS (ref. 12). DSMs can be regarded as parent materials of Weyl semimetals (WSMs). When either time-reversal symmetry (TRS) or space-inversion symmetry is broken, DSMs evolve into WSMs[13,14] due to lifted spin degeneracy. Remarkable characteristics of the Weyl state include surface Fermi arcs connecting Weyl points[15] and the chiral anomaly, which originates from charge pumping between Weyl points with opposite chirality and is manifested as negative longitudinal magnetoresistance (LMR)[16–18]. WSMs generated by the broken space-inversion symmetry were first experimentally realized in TaAs-class materials[19–23] and photonic crystals[24]. A Weyl state due to spontaneous TRS breaking was recently reported in $YbMnBi_2$ (ref. 25) and its TRS breaking is suggested to be caused by a net ferromagnetic (FM) component of a canted antiferromagnetic (CAFM) state[25].

In this article, we report the first observation of relativistic fermion behaviour in a material showing ferromagnetic properties, that is, $Sr_{1-y}Mn_{1-z}Sb_2$ ($y, z < 0.1$). We observed strong Shubnikov–de Haas (SdH) and de Haas–van Alphen (dHvA) oscillations in this material. The analyses of the SdH and dHvA oscillations demonstrate that this material harbours nearly massless relativistic fermions ($m^* = 0.04–0.05m_0$) along with a non-trivial Berry phase. Neutron scattering measurements reveal a FM transition at 565 K, followed by a transition at 304 K to a CAFM with a net FM component, similar to the predicted CAFM state for $YbMnBi_2$ (ref. 25). These findings make $Sr_{1-y}Mn_{1-z}Sb_2$ a promising candidate for investigating the effect of TRS breaking on the electronic band structure.

$SrMnSb_2$ is closely related to $AMnBi_2$ (A = Sr, Ca, Eu or Yb), as these materials exhibit fascinating properties that have origins in their structural building blocks, namely, the 2D Bi square net that harbours relativistic fermions. $SrMnBi_2$ and $CaMnBi_2$ possess anisotropic Dirac cone states[26,27]; $EuMnBi_2$ was recently found to show a quantum Hall effect due to the magnetically confined 2D Dirac fermions[28], and $YbMnBi_2$ displays a TRS-breaking Weyl state due to the lifted spin degeneracy caused by the FM component of a CAFM state[25]. Given that the 2D Bi square net can host relativistic fermions, one natural expectation is that the 2D Sb network in $SrMnSb_2$ may also host relativistic fermions. One advantage of $SrMnSb_2$ is that the Sb 2D network should have weaker spin–orbital coupling (SOC) than the Bi square net, which might reduce or close the SOC-induced gap near the Dirac point, making it easy to observe exotic phenomena related to massless Dirac fermions[29,30]. This idea serves as the motivating principle for our work.

We synthesized plate-like single crystals of $Sr_{1-y}Mn_{1-z}Sb_2$ (y, $z < 0.1$) (see the inset to Fig. 1a) using a self-flux method (see the Methods). Single-crystal neutron scattering measurements reveal that the synthesized material crystallizes in an orthorhombic structure with space group *Pnma*, similar to the previously reported structure of $SrMnSb_2$ (ref. 31). No structural transition was observed down to 5 K. The lattice and other structural parameters

---

[1]Department of Physics and Engineering Physics, Tulane University, New Orleans, Louisiana 70018, USA. [2]Department of Physics and Astronomy, Louisiana State University, Baton Rouge, Louisiana 70803, USA. [3]Oak Ridge National Laboratory, Oak Ridge, Tennessee 37831, USA. [4]National High Magnetic Field Laboratory, Tallahassee, Florida 32310, USA. [5]Department of Physics and Advanced Materials Research Institute, University of New Orleans, New Orleans, Louisiana 70148, USA. [6]Shanghai Institute of Ceramics, Chinese Academy of Sciences, Shanghai 200050, China. [7]Los Alamos National Laboratory, Los Alamos, New Mexico 87545, USA. [8]Department of Physics, Florida State University, Tallahassee, Florida 32306, USA. [†]These authors contributed equally to this work. *e-mail: zmao@tulane.edu

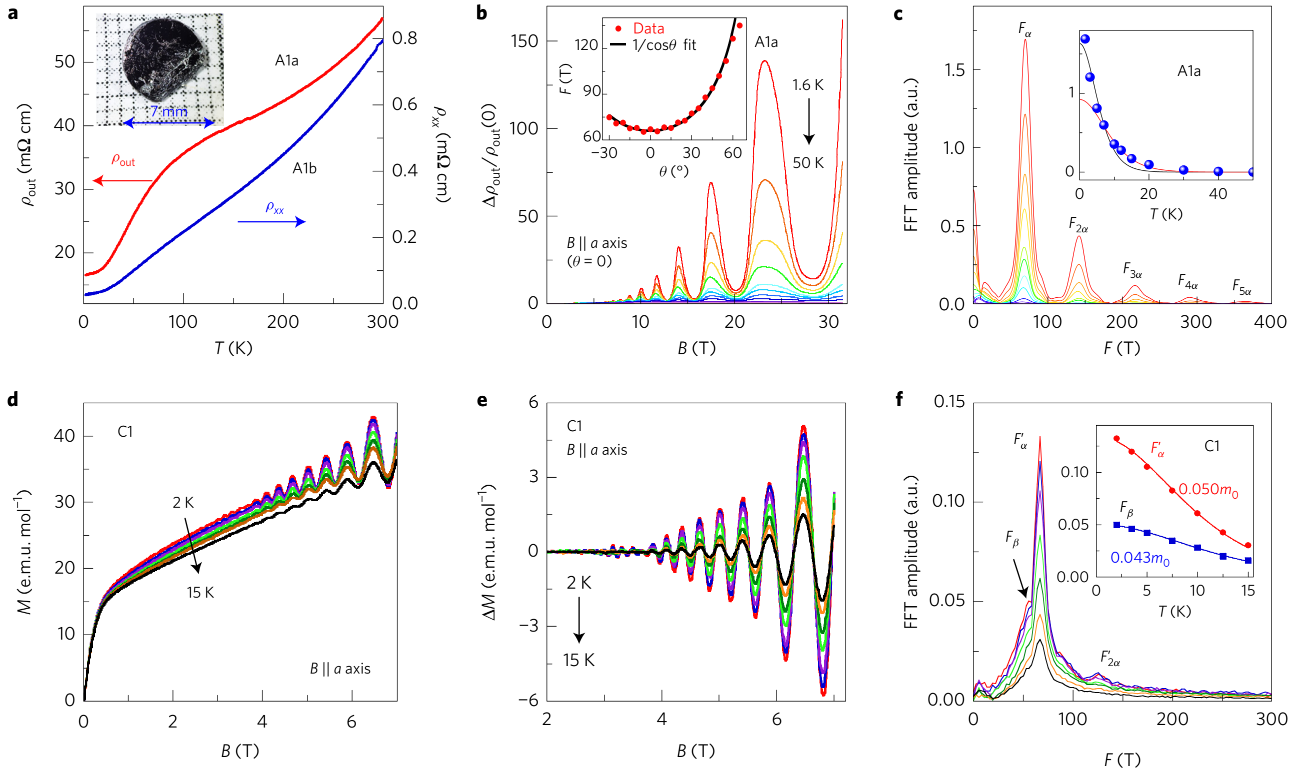

Figure 1 | Quantum oscillations in $Sr_{1-y}Mn_{1-z}Sb_2$. **a**, In-plane (ρ_{xx}) and out-of-plane (ρ_{out}) resistivity as a function of temperature, with ρ_{xx} (300 K)/ρ_{xx} (2 K) ∼ 29 and $\rho_{out}/\rho_{xx} \sim 609$ at 2 K; inset, an optical image of a large single crystal. **b**, The out-of-plane magnetoresistivity, $\Delta\rho_{out}/\rho_{out} = [\rho_{out}(B) - \rho_{out}(0)]/\rho_{out}(0)$, as a function of magnetic field at various temperatures (1.6, 3.0, 5.0, 7.0, 10.0, 12.0, 15.0, 20.0, 30.0, 40.0 and 50.0 K), which shows strong SdH oscillations. Inset, the angular dependence of the SdH oscillation frequency $F(\theta)$ with $\theta = 0°$ corresponding to the field aligned along the out-of-plane [100] direction; $F(\theta)$ can be fitted by $F_0/\cos\theta$, suggesting a quasi-2D Fermi surface. **c**, The FFT spectra of $\Delta\rho_{out}(B)$ at various temperatures (1.6, 3, 5, 7, 10, 12, 15, 20, 30, 40 and 50 K). $F_{2\alpha}$, $F_{3\alpha}$, $F_{4\alpha}$ and $F_{5\alpha}$ represent harmonic peaks. The inset shows the temperature dependence of the FFT amplitude normalized by ρ_{out} ($B = 0$). The solid black and red curves represent the fits of the LK formula to the 2–50 K and 7–50 K temperature ranges respectively, which do not appear to be satisfactory (see text). **d**, Isothermal magnetization at various temperatures (2.0, 3.5, 5.0, 7.5, 10.0, 12.5 and 15.0 K), showing strong dHvA oscillations. **e**, Oscillatory component of magnetization ΔM at various temperatures (2.0, 3.5, 5.0, 7.5, 10.0, 12.5 and 15.0 K). **f**, FFT spectra of ΔM at various temperatures (2.0, 3.5, 5.0, 7.5, 10.0, 12.5 and 15.0 K). The inset shows the fits of the temperature dependence of the dHvA FFT amplitudes to the LK formula from which the quasi-particles are found to be nearly massless.

obtained from the neutron diffraction refinement are presented in Supplementary Note 1. The compositions of our single crystals were analysed using an energy-dispersive X-ray spectrometer, which shows that the actual composition involves Mn and Sr deficiency as described by $Sr_{1-y}Mn_{1-z}Sb_2$ (y, $z < 0.1$). Interestingly, the Mn and Sr non-stoichiometry were found to have a strong effect on the magnetic properties of $Sr_{1-y}Mn_{1-z}Sb_2$. Samples with larger Sr deficiency ($y \sim 0.08$, $z \sim 0.02$) display stronger FM behaviour, while weaker FM behaviour occurs in samples with enhanced Mn deficiency ($y \sim 0.01$–0.04. $z \sim 0.04$–0.1). According to the magnitude of the FM saturated moment M_s, we categorize our samples into three types; $M_s \sim 0.1$–$0.6\mu_B$/Mn for type A, 0.04–$0.06\mu_B$/Mn for type B and 0.004–$0.006\mu_B$/Mn for type C. Detailed comparisons of magnetic properties between type A, B and C samples will be given below. All samples used in this study were first screened through magnetization measurements and labelled with different numbers (for example, A1, A2). Then we cleaved each screened crystal to small pieces for various measurements and label each small piece by adding a lowercase letter (for example, A1a, A1b).

We will first present the electronic transport properties of type A samples and compare them with those of type B and C samples. All of the transport data presented in Figs 1a–c and 2a–e were collected on type A samples. As seen in Fig. 1a, both in-plane (ρ_{xx}) and out-of-plane (ρ_{out}) resistivity exhibit metallic temperature dependences, with the in-plane residual resistivity ratio ρ_{xx} (300 K)/ρ_{xx} (2 K) being ∼29. The ρ_{out}/ρ_{xx} ratio increases markedly with decreasing temperature and reaches 609 at 2 K, suggesting quasi-2D electronic band structure. We conducted both in-plane and out-of-plane (that is, [100]) magnetotransport measurements for a type A sample. The magnetoresistivity (MR $= [\rho(B) - \rho(0)]/\rho(0)$) along both directions exhibit strong SdH oscillations for $T < 30$ K. We present the out-of-plane MR data in Fig. 1b and the in-plane MR data are given in Supplementary Note 2. We find that the relative oscillation amplitude $\Delta\rho_{out}/\rho_{avg}$ is considerably large, reaching 100% near 23 T at 1.6 K. A large SdH oscillation amplitude is consistent with a quasi-2D electronic structure[32]. Furthermore, we also performed pulsed field measurements for fields up to 65 T for ρ_{out} and observed signatures of Zeeman splitting, as shown in Supplementary Fig. 3, from which the Landé factor is estimated to 6.7 (see Supplementary Note 3). In addition to SdH oscillations, we also observed dHvA oscillations in $Sr_{1-y}Mn_{1-z}Sb_2$ in magnetization measurements by a superconducting quantum interference device (SQUID) magnetometer. Type C samples exhibit the largest oscillation amplitude (up to 5 e.m.u. mol^{-1} near 6.5 T) due to their relatively weak FM background, as shown in Fig. 1d,e.

The fast Fourier transformation (FFT) analyses of the oscillatory resistivity $\Delta\rho_{out}$ (Fig. 1c) and $\Delta\rho_{xx}$ (Supplementary Fig. 2b) show that the oscillation frequencies are ∼69.6 T and 70.1 T, respectively. The field was about 20° misaligned relative to the [100] axis for both $\rho_{out}(B)$ and $\rho_{xx}(B)$ measurements. When the field was exactly aligned along [100], the frequency drops to 67 T (see the inset to Fig. 1b). While the SdH oscillations show only a single frequency, the FFT

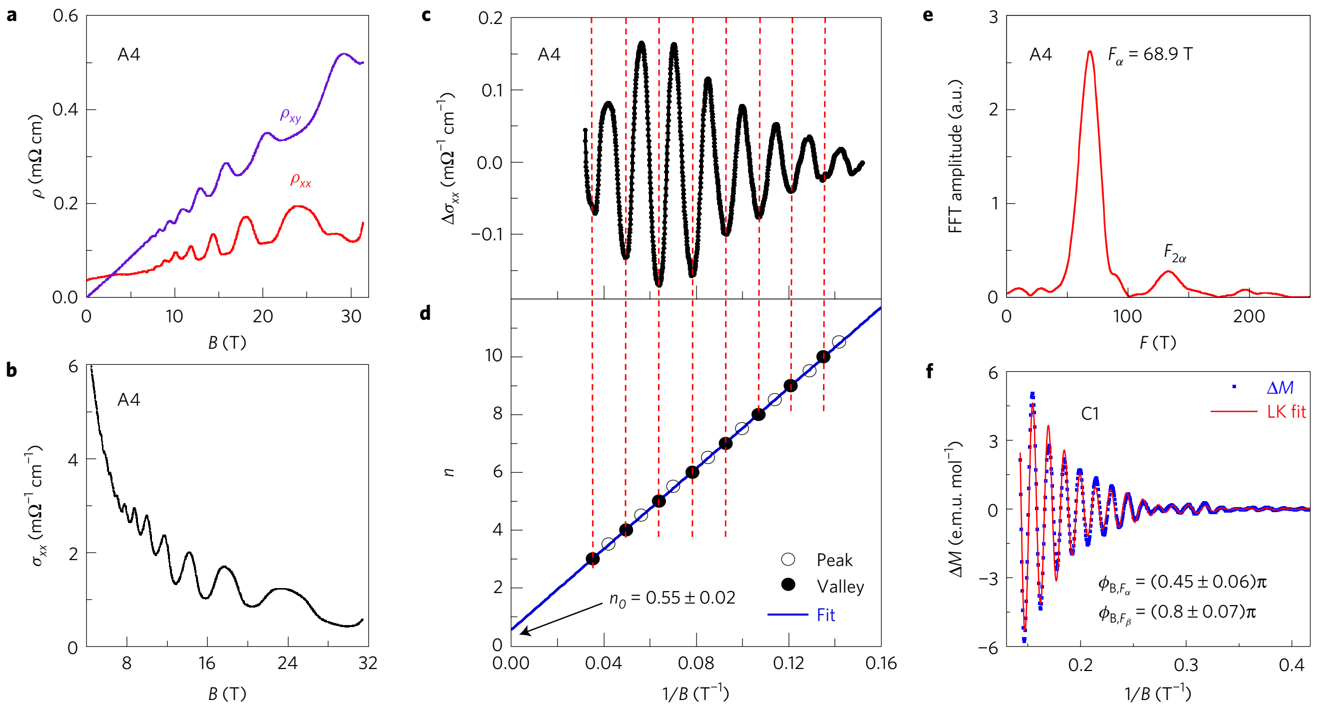

Figure 2 | Non-trivial Berry phase of realistic fermions in $Sr_{1-y}Mn_{1-z}Sb_2$. a, The in-plane longitudinal (ρ_{xx}) and the transverse (Hall) (ρ_{xy}) resistivity as a function of magnetic field measured at 2 K on an identical sample A4; both ρ_{xx} and ρ_{xy} show strong SdH oscillations. **b**, The in-plane conductivity σ_{xx} converted from the ρ_{xx} and ρ_{xy} data shown in **a** using $\sigma_{xx} = \rho_{xx}/(\rho_{xx}^2 + \rho_{xy}^2)$ for sample A4. **c**, The in-plane oscillatory conductivity $\Delta\sigma_{xx}$ versus $1/B$ at 2 K. **d**, The Landau Level (LL) index fan diagram derived from the oscillatory conductivity at 2 K of sample A4. The integer LL indices (n) are assigned to the minima of $\Delta\sigma_{xx}$ (refs 36,37). The intercept n_0 on the n axis obtained from the extrapolation of the best linear fit in the fan diagram is 0.55 ± 0.02, suggesting that the π Berry phase accumulated in the cyclotron orbits. **e**, FFT spectra of the in-plane conductivity σ_{xx} at 2 K for sample A4. **f**, The fit of the dHvA oscillation pattern at 2 K to the LK formula (see the Methods) for sample C1, from which non-trivial Berry phases are also obtained.

spectra of the dHvA oscillations (Fig. 1f) reveal two frequencies, $F'_\alpha = 66.7$ T and $F_\beta = 53.3$ T. The inconsistency between SdH and dHvA oscillations is often seen in low-dimensional materials such as layered organic conductors[32] and originates from the different mechanisms of SdH and dHvA oscillations. SdH oscillations originate from the oscillating scattering rate and can thus be complicated by the detailed scattering mechanisms. This in some cases leads the observed resistivity oscillations to substantially deviate from the prediction by the Lifshitz–Kosevich (LK) theory[32], which is the case for $Sr_{1-y}Mn_{1-z}Sb_2$ as discussed below. By contrast, the dHvA effect is caused directly by the oscillations of electrons' free energy and can be well described by the LK model for both 3D and 2D cases[32]. As a result, the dHvA effects can provide more direct information on the Fermi surface for 2D-like materials such as $Sr_{1-y}Mn_{1-z}Sb_2$.

We evaluated the extremal cross-sectional area A_F of the Fermi surface using the Onsager relation $F = (\Phi_0/2\pi^2)A$. The frequency of 67 T corresponds to $A_F = 0.64(0)$ nm^{-2}, about one-half of A_F (=1.45 nm^{-2}) probed in the same field configuration for $SrMnBi_2$ (ref. 26). Such a small value of A_F indicates a small Fermi surface. Moreover, we also examined the dependence of F on the magnetic field-orientation angle θ via measuring SdH oscillations under various field orientations (Supplementary Fig. 4). As shown in the inset to Fig. 1b, $F(\theta)$ can be fitted with a $F_0/\cos\theta$ function, suggesting that the Fermi surface responsible for the SdH oscillations in $Sr_{1-y}Mn_{1-z}Sb_2$ is quasi-2D. A remarkable signature of quantum oscillations of a low-dimensional system is the large oscillation amplitude as noted above. The second frequency component F_β probed in the dHvA oscillations suggests that the Fermi surface of $Sr_{1-y}Mn_{1-z}Sb_2$ is warped.

In general, the effective mass m^* of quasi-particles on the Fermi pocket can be obtained from the fit of the temperature dependence of the FFT amplitude of the SdH/dHvA oscillations by the temperature damping factor of the LK equation, that is, $R_T = \alpha T m^*/[m_0 B \sinh(\alpha T m^*/m_0 B)]$, where $\alpha = (2\pi^2 k_B m_0)/(\hbar e)$. However, as seen in the inset of Fig. 1c and Supplementary Fig. 2c, the LK formula barely fits the SdH FFT amplitude data due to the steep increase of the oscillation amplitude below 7 K (see the black fitted curve), which is not surprising since the LK theory cannot precisely describe SdH oscillations in low-dimensional systems in many cases as indicated above. If the data points below 7 K are not included in the fit, a better fit can be obtained (the red fitted curve in the inset to Fig. 1c), which yields $m^* = 0.14m_0$. The effective mass obtained in such a way is rough since the fit does not cover all of the data points. In contrast, accurate m^* can be found from the fit of the temperature dependence of the dHvA FFT amplitude to the LK formula. As seen in the inset to Fig. 1f, all of the dHvA oscillation FFT amplitude data points can be fitted, which yields $m^* = 0.050m_0$ for F'_α and $0.043m_0$ for F_β, comparable to that of the gapless Dirac semimetal Cd_3As_2 ($m^* = 0.023$–$0.044m_0$) (refs 8,33,34), implying that $Sr_{1-y}Mn_{1-z}Sb_2$ most likely harbours relativistic fermions.

To seek further evidence for relativistic fermions in $Sr_{1-y}Mn_{1-z}Sb_2$, we examined the Berry phase ϕ_B accumulated along cyclotron orbits. For a Dirac/Weyl system, pseudo-spin rotation under a magnetic field should result in a non-trivial Berry phase, which can be accessed from the Landau level (LL) index fan diagram or the direct fit of the SdH/dHvA oscillation pattern to the LK formula. For a 2D or quasi-2D system with relativistic fermions, the intercept n_0 on the n axis of the LL fan diagram is expected to be 1/2 (ref. 35), for which the corresponding Berry phase is $2\pi n_0 = \pi$. In Fig. 2d, we present the LL fan diagram established using the oscillatory conductivity $\Delta\sigma_{xx}$ data (Fig. 2c), which is obtained by subtracting the background from the conductivity σ_{xx} (Fig. 2b). σ_{xx} is converted from the longitudinal resistivity ρ_{xx} and the transverse (Hall) resistivity ρ_{xy} data collected on an identical sample A4

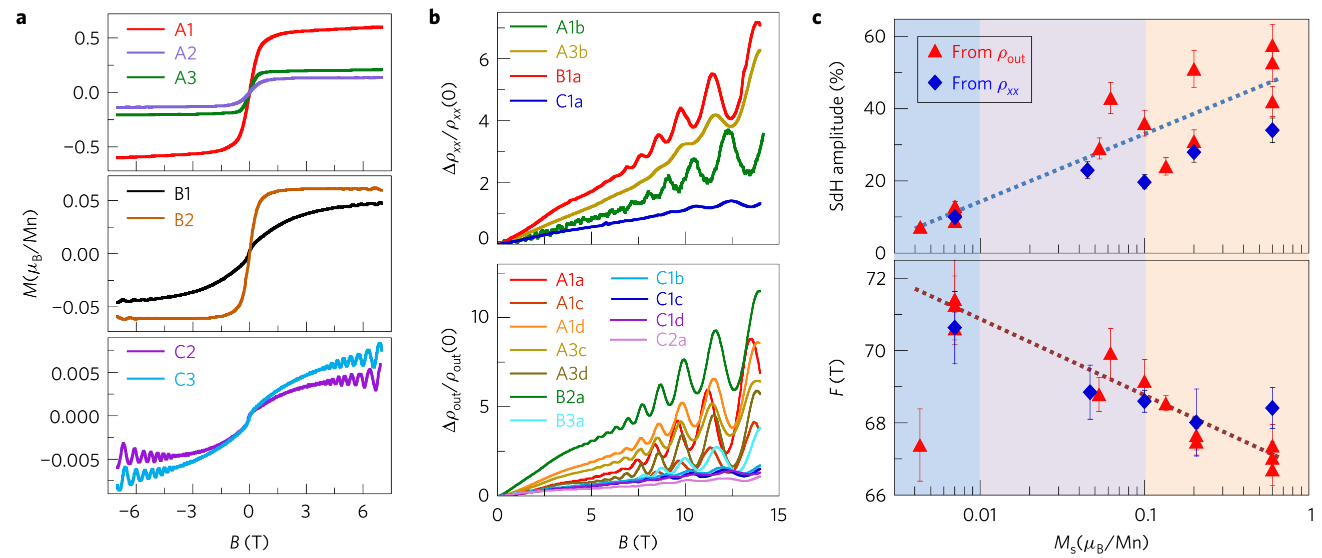

Figure 3 | Coupling between magnetism and quantum transport properties in Sr$_{1-y}$Mn$_{1-z}$Sb$_2$. a, Field sweeps of magnetization at 5 K for type A samples (showing significant FM behaviour, see the upper panel), type B samples (showing relatively weak FM behaviour, see the middle panel), and type C samples (displaying very weak FM behaviour, see the bottom panel). All of these samples exhibit dHvA oscillations. dHvA oscillations of type A and B samples are observable only when the data are zoomed in (see Supplementary Fig. 5d). **b**, SdH oscillations of ρ_{xx} (upper panel) and ρ_{out} (lower panel) of type A, B and C samples. All of these data were collected in the 14 T PPMS system and the fields were roughly aligned along the [100] axis, with the misalignment angle <10°; the relative shift of the oscillation pattern between samples is due to the field misalignment. **c**, The relative SdH oscillation amplitude near 12.5 T (upper panel) and the SdH oscillation frequency (lower panel) as a function of the FM saturation moment M_{s} for type A, B and C samples. The error bars of the frequencies are obtained from the linear fits of the LL fan diagrams, representing the uncertainties of the fitted slopes. The error bars of the SdH oscillation amplitudes represent the peak and valley amplitude difference near 12.5 T, about 10% of the averaged amplitude. A general trend of increased oscillation amplitude and decreased oscillation frequency with increasing M_{s} can be observed, as denoted by the dashed lines.

(Fig. 2a) using $\sigma_{xx} = \rho_{xx}/(\rho_{xx}^2 + \rho_{xy}^2)$. Following the customary practice of defining the LL index[36,37], we assigned integer LL indices to the minima of $\Delta\sigma_{xx}$ as illustrated in Fig. 2c,d. As seen in Fig. 2d, the intercept n_0 on the n axis we obtained from the extrapolation of the best linear fit in the fan diagram is 0.55 ± 0.02, close to the expected value of 0.5 for a 2D or quasi-2D system with relativistic fermions. The frequency obtained from the fit is 69.8 T, only about 1% higher than the frequency (68.9 T) obtained from the FFT analyses of σ_{xx} (Fig. 2e), which should be considered as a reliable metric for the linear fit in the fan diagram (note that the field is ∼5° misaligned along [100] for ρ_{xx} and ρ_{xy} measurements shown in Fig. 2a). Therefore, our result of the intercept $n_0 = 0.55 \pm 0.02$ obtained on the A4 sample can be considered to be strong evidence of the π Berry phase of relativistic fermions in Sr$_{1-y}$Mn$_{1-z}$Sb$_2$. This is further verified by the LL fan diagram analyses on two other samples (see Supplementary Note 5) as well as by our direct fit of the dHvA oscillation pattern to the LK formula that takes the Berry phase into account for a Dirac system (see the Methods). As seen in Fig. 2f, the Berry phases extracted from the dHvA oscillation pattern fit are (0.45 ± 0.06)π and (0.8 ± 0.07)π, respectively, for the F'_α and F_β components, which are clearly non-trivial. The sample difference in non-stoichiometry composition may lead to slight difference in Fermi surface morphology, which may explain the discrepancy in ϕ_{B} probed in these two different approaches. Additionally, the positive sign of R_{H} (Fig. 2a) indicates that the dominant charge carriers responsible for quantum oscillations are hole-like.

Besides relativistic fermion behaviour, Sr$_{1-y}$Mn$_{1-z}$Sb$_2$ exhibits FM properties as mentioned above, in contrast with the AMnBi$_2$ materials with Dirac/Weyl fermions[25,26,28,38], for which no ferromagnetism has been reported. To examine whether the relativistic fermion transport is coupled with ferromagnetism in Sr$_{1-y}$Mn$_{1-z}$Sb$_2$, we have measured the magnetotransport properties of several groups of samples with different magnitudes of magnetic moment. Before we compare the quantum transport properties among those samples, we will first discuss the origin of ferromagnetism in Sr$_{1-y}$Mn$_{1-z}$Sb$_2$. In the top panel of Fig. 3a, we show the isothermal magnetization data at 5 K for three typical type A samples that exhibit relatively strong FM behaviour with $M_{\text{s}} \sim 0.14$–$0.6\mu_{\text{B}}$/Mn for the magnetic field along the [100] direction. We also measured the temperature dependence of the magnetization and found that the FM polarization occurs even at 400 K (Supplementary Fig. 6). To understand the nature of such FM behaviour, we performed single-crystal neutron diffraction measurements using a type A sample with $M_{\text{s}} \sim 0.2\mu_{\text{B}}$ at 5 K. We found that Sr$_{1-y}$Mn$_{1-z}$Sb$_2$ exhibits complex magnetic states. First, a long-range FM order with Mn moments along the b axis occurs below $T_{\text{C}} = 565$ K (Fig. 4b). Figure 4a shows the temperature dependence of the FM scattering intensity that overlaps with the nuclear scattering intensity at the (200) reflection, from which a clear FM transition around 565 K can be seen, consistent with the FM polarization behaviour up to 400 K in the magnetization measurements (Supplementary Fig. 6). The calculated FM ordered Mn moment along the b axis at 350 K is $\sim 0.28(6)\mu_{\text{B}}$/Mn. Second, the FM order parameter shows an unusual decrease below 300 K, coinciding with the presence of a strong AFM order below 304 K, as seen in the temperature dependence of the (001) magnetic peak intensity in Fig. 4c. Both the magnetic and nuclear structures are determined from the refinement of the neutron diffraction data collected at 5 K. A C-type AFM structure was found to best fit the data. In consideration of the existence of ferromagnetism below T_{N} as observed from the magnetization and the (200) nuclear intensity being higher than that above 565 K, we conclude that the ground state in the type A sample should be a CAFM state (Fig. 4d). The nearest-neighbour Mn spins with moments of $\sim 3.77(9)\mu_{\text{B}}$ are aligned antiparallel within the b–c plane and aligned parallel along the a axis. The canting leads to a FM component along the b axis, with the size of moment of $\sim 0.2\mu_{\text{B}}$, as seen from the magnetization

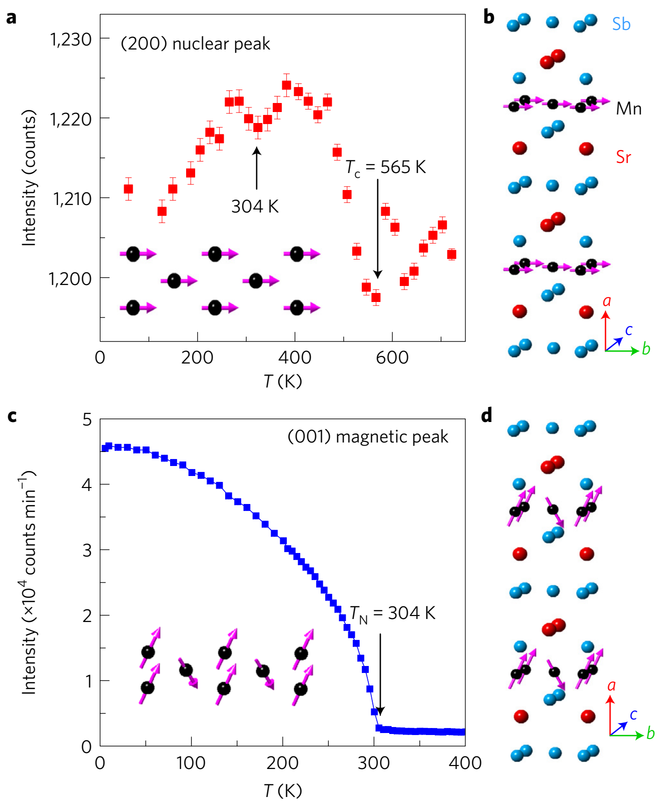

Figure 4 | Magnetism of $Sr_{1-y}Mn_{1-z}Sb_2$. a, The temperature dependence of the neutron diffraction intensity at (200) obtained with a counting time of 10 min per point. The error bar uses the standard deviation, that is, square root of the total counts. Inset, the FM magnetic structure of the Mn sublattice, viewed from the (101) direction. The Mn moments are aligned along the *b* axis. **b**, The magnetic structure of the FM state for $304\,K < T < 565\,K$. **c**, Temperature dependence of the AFM order parameter (that is, the (001) magnetic peak intensity). The error bars are smaller than the symbols so that they cannot be viewed on this scale. Inset, the canted AFM magnetic structure of the Mn sublattice, viewed from the (101) direction. A net FM component is due to the canting of magnetic moment along the *b* axis. **d**, The *C*-type AFM magnetic structure in the AFM state for $T < 304\,K$.

measurements. Details of the magnetic structure refinement are given in Supplementary Note 7.

It is worth pointing out that the *C*-type CAFM state probed in $Sr_{1-y}Mn_{1-z}Sb_2$ is analogous to the CAFM state expected for $YbMnBi_2$ (ref. 25) whose FM component is believed to be responsible for the TRS-breaking Weyl state[25], although recent neutron scattering experiments did not resolve such a CAFM state in $YbMnBi_2$ (refs 39,40). Given that $Sr_{1-y}Mn_{1-z}Sb_2$ shares a similar layered structure with $YbMnBi_2$ and exhibits coexistence of relativistic fermions and ferromagnetism as discussed above, there is a possibility that the FM component in this material might result in a TRS-breaking Weyl state, which is yet to be clarified by further experimental and theoretical studies. As indicated above, one remarkable signature of a Weyl state is a chiral anomaly, which is manifested as negative LMR. For $Sr_{1-y}Mn_{1-z}Sb_2$, we have indeed observed negative LMR in some type A samples with the current along the [100] direction (see Supplementary Note 8). As shown in Supplementary Fig. 8, the field and field-orientation dependences of the LMR, as well as the B^2 dependence of magnetoconductance, appear to be in line with the chiral anomaly effect. However, these phenomena have not been observed in in-plane magnetotransport measurements. Therefore, it is unclear whether the observed negative LMR is associated with chiral anomaly. Although $Sr_{1-y}Mn_{1-z}Sb_2$ shows FM properties, the negative LMR seen in our experiments should not be due to magnetic scattering, since the magnetoconductance continues to follow B^2 dependence even when the magnetization becomes saturated above 2 T (Supplementary Fig. 8c).

Next we compare the quantum transport properties of the samples with different FM components (Fig. 3b). As summarized in the top panel of Fig. 3c, the relative SdH oscillation amplitude exhibits a remarkable enhancement with the increase of the FM saturated moment M_S for both ρ_{xx} and ρ_{out}, from ~10% for type C to ~25–45% for type B, and ~20–60% for type A samples. Coincidentally, the SdH oscillation frequency *F* statistically decreases with increasing M_S, except for a large deviation of one data point collected on a type C sample that is probably caused by sample inhomogeneity (Fig. 3c, bottom panel). In general, disorder is expected to suppress quantum oscillations, but the suppression of SdH oscillations in type B or C samples cannot be understood in terms of increased disorder. This is most clearly seen by examining the lack of correlations between the residual resistivity ratio RRR (which characterizes the disorder level) and the relative SdH oscillation amplitude as demonstrated in Supplementary Fig. 9. In $Sr_{1-y}Mn_{1-z}Sb_2$ the disorder induced by Sr and Mn vacancies is separated from the 2D Sb conduction layers and is expected to have only a weak effect on the in-plane cyclotron motion. This idea also accounts for the insensitivity of quantum oscillations to disorder in this material system.

Our observations of enhanced SdH oscillations in the samples with stronger ferromagnetism suggest an enhanced carrier mobility in those samples. The correlation of ferromagnetism and mobility in $Sr_{1-y}Mn_{1-z}Sb_2$ might be understood in terms of the change in band structure driven by ferromagnetism. Indeed, this has been shown to be the case for $YbMnBi_2$ by first-principle calculations[25]. Here, the spin degeneracy can be lifted by a FM component arising from the formation of a CAFM state. The relative shift of the bands in the magnetically ordered state closes the SOC-induced gap leading to the formation of Weyl nodes. In $Sr_{1-y}Mn_{1-z}Sb_2$, our observation of a decrease in the quantum oscillation frequency *F* caused by enhanced ferromagnetism appears to support the gap-closing scenario due to TRS breaking. As seen in Fig. 3c, *F* decreases from ~72 T to ~67 T when M_s increases by two orders of magnitude from type C to A samples, which corresponds to a ~7% shrinking of the cross-section area of Fermi surface. Such a decrease in the quantum oscillation frequency accompanied by the simultaneous increase of quantum mobility with increasing M_s implies that the TRS breaking plays a role in modifying band structure.

Finally, we discuss the inconsistency between our experimental observations and the early density functional theory (DFT) calculation results[29]. These calculations predict that the orthorhombic structural distortion in $SrMnSb_2$ causes the absence of a Dirac band crossing near the Fermi level. Instead, the distortion is thought to cause a rather large gap (~1 eV) to form at momentum points where Dirac crossing is expected. However, this gap is expected to close if the unit cell volume shrinks by 10% as it would under external pressure[29]. We note that the structural parameters used in the DFT calculations[29] were taken from a previous report[31] and these lattice parameters differ slightly from our structural parameters probed by neutron scattering (see Supplementary Table 1). In fact, the unit cell volume of our sample is 2% less than that of the previously reported sample[31], with the difference most likely induced by the Sr and Mn deficiencies. The chemical pressure due to Sr and Mn vacancies, while not large enough to close the ~1 eV gap, can possibly lead to the closing of a smaller gap (~0.2 eV) near Y points at the Brillouin zone boundary. Since the band dispersion near Y is quasi-linear[29], a Dirac band crossing at Y may occur when the gap closes due to chemical pressure and TRS breaking. Indeed, Dirac band crossing near Y was observed in angle-resolved photoemission spectroscopy measurements on $YbMnBi_2$ (ref. 25). Given the structural similarity between $YbMnBi_2$ and $Sr_{1-y}Mn_{1-z}Sb_2$, it is reasonable to expect similar Dirac crossings near Y in $Sr_{1-y}Mn_{1-z}Sb_2$. Although the DFT calculations did not give a result consistent with our experimental observations for $SrMnSb_2$, their prediction of Dirac fermion behaviour in tetragonal $BaMnSb_2$ at ambient pressure has been demonstrated in recent experiments[30,41]. The Dirac fermions in $BaMnSb_2$ are also nearly massless ($m^* \sim 0.050–0.052 m_0$). However, $BaMnSb_2$ does not display FM order above room temperature, instead ordering in a *G*-type AFM structure below 283 K. This AFM order is in contrast with the striking FM properties seen in type A samples of $Sr_{1-y}Mn_{1-z}Sb_2$. The coexistence of nearly massless Dirac fermions and ferromagnetism in $Sr_{1-y}Mn_{1-z}Sb_2$ offers a unique platform for exploring the effect of TRS breaking on Dirac bands and seeking a possible magnetic Weyl state.

Methods

Methods, including statements of data availability and any associated accession codes and references, are available in the online version of this paper.

Received 9 August 2015; accepted 28 June 2017;

References

1. Wang, Z. *et al*. Dirac semimetal and topological phase transitions in A_3Bi(A = Na, K, Rb). *Phys. Rev. B* **85,** 195320 (2012).
2. Liu, Z. K. *et al*. Discovery of a three-dimensional topological Dirac semimetal, Na_3Bi. *Science* **343,** 864–867 (2014).
3. Wang, Z., Weng, H., Wu, Q., Dai, X. & Fang, Z. Three-dimensional Dirac semimetal and quantum transport in Cd_3As_2. *Phys. Rev. B* **88,** 125427 (2013).
4. Liu, Z. K. *et al*. A stable three-dimensional topological Dirac semimetal Cd_3As_2. *Nat. Mater.* **13,** 677–681 (2014).
5. Neupane, M. *et al*. Observation of a three-dimensional topological Dirac semimetal phase in high-mobility Cd_3As_2. *Nat. Commun.* **5,** 3786 (2014).
6. Borisenko, S. *et al*. Experimental realization of a three-dimensional Dirac semimetal. *Phys. Rev. Lett.* **113,** 027603 (2014).
7. Liang, T. *et al*. Ultrahigh mobility and giant magnetoresistance in the Dirac semimetal Cd_3As_2. *Nat. Mater.* **14,** 280–284 (2015).
8. Narayanan, A. *et al*. Linear magnetoresistance caused by mobility fluctuations in *n*-doped Cd_3As_2. *Phys. Rev. Lett.* **114,** 117201 (2015).
9. Li, Q. *et al*. Chiral magnetic effect in $ZrTe_5$. *Nat. Phys.* **12,** 550–554 (2016).
10. Bian, G. *et al*. Topological nodal-line fermions in spin–orbit metal $PbTaSe_2$. *Nat. Commun.* **7,** 10556 (2016).
11. Wu, Y. *et al*. Dirac node arcs in $PtSn_4$. *Nat. Phys.* **12,** 667–671 (2016).
12. Schoop, L. M. *et al*. Dirac cone protected by non-symmorphic symmetry and three-dimensional Dirac line node in ZrSiS. *Nat. Commun.* **7,** 11696 (2016).
13. Huang, S.-M. *et al*. A Weyl Fermion semimetal with surface Fermi arcs in the transition metal monopnictide TaAs class. *Nat. Commun.* **6,** 7373 (2015).
14. Weng, H., Fang, C., Fang, Z., Bernevig, B. A. & Dai, X. Weyl semimetal phase in noncentrosymmetric transition-metal monophosphides. *Phys. Rev. X* **5,** 011029 (2015).
15. Wan, X., Turner, A. M., Vishwanath, A. & Savrasov, S. Y. Topological semimetal and Fermi-arc surface states in the electronic structure of pyrochlore iridates. *Phys. Rev. B* **83,** 205101 (2011).
16. Nielsen, H. B. & Ninomiya, M. The Adler-Bell-Jackiw anomaly and Weyl fermions in a crystal. *Phys. Lett. B* **130,** 389–396 (1983).
17. Son, D. T. & Spivak, B. Z. Chiral anomaly and classical negative magnetoresistance of Weyl metals. *Phys. Rev. B* **88,** 104412 (2013).
18. Jho, Y.-S. & Kim, K.-S. Interplay between interaction and chiral anomaly: anisotropy in the electrical resistivity of interacting Weyl metals. *Phys. Rev. B* **87,** 205133 (2013).
19. Yang, L. X. *et al*. Weyl semimetal phase in the non-centrosymmetric compound TaAs. *Nat. Phys.* **11,** 728–732 (2015).
20. Xu, S.-Y. *et al*. Discovery of a Weyl fermion semimetal and topological Fermi arcs. *Science* **349,** 613–617 (2015).
21. Xu, N. *et al*. Observation of Weyl nodes and Fermi arcs in tantalum phosphide. *Nat. Commun.* **7,** 11006 (2015).
22. Lv, B. Q. *et al*. Experimental discovery of Weyl semimetal TaAs. *Phys. Rev. X* **5,** 031013 (2015).
23. Xu, S.-Y. *et al*. Discovery of a Weyl fermion state with Fermi arcs in niobium arsenide. *Nat. Phys.* **11,** 748–754 (2015).
24. Lu, L. *et al*. Experimental observation of Weyl points. *Science* **349,** 622–624 (2015).
25. Borisenko, S. *et al*. Time-reversal symmetry breaking type-II Weyl state in $YbMnBi_2$. Preprint at http://arxiv.org/abs/1507.04847 (2015).
26. Park, J. *et al*. Anisotropic Dirac fermions in a Bi square net of $SrMnBi_2$. *Phys. Rev. Lett.* **107,** 126402 (2011).
27. Feng, Y. *et al*. Strong anisotropy of Dirac cones in $SrMnBi_2$ and $CaMnBi_2$ revealed by angle-resolved photoemission spectroscopy. *Sci. Rep.* **4,** 05385 (2014).
28. Masuda, H. *et al*. Quantum Hall effect in a bulk antiferromagnet $EuMnBi_2$ with magnetically confined two-dimensional Dirac fermions. *Sci. Adv.* **2,** e1501117 (2016).
29. Farhan, M. A., Geunsik, L. & Ji Hoon, S. $AEMnSb_2$ (AE = Sr, Ba): a new class of Dirac materials. *J. Phys. Condens. Matter* **26,** 042201 (2014).
30. Liu, J. *et al*. Nearly massless Dirac fermions hosted by Sb square net in $BaMnSb_2$. *Sci. Rep.* **6,** 30525 (2016).
31. Brechtel, E., Cordier, G. & Schäfer, H. Neue ternäre erdalkali-übergangselement-pnictide. *J. Less-Common Met.* **79,** 131–138 (1981).
32. Kartsovnik, M. V. High magnetic fields: a tool for studying electronic properties of layered organic metals. *Chem. Rev.* **104,** 5737–5782 (2004).
33. He, L. P. *et al*. Quantum transport evidence for the three-dimensional Dirac semimetal phase in Cd_3As_2. *Phys. Rev. Lett.* **113,** 246402 (2014).
34. Zhao, Y. *et al*. Anisotropic Fermi surface and quantum limit transport in high mobility three-dimensional Dirac semimetal Cd_3As_2. *Phys. Rev. X* **5,** 031037 (2015).
35. Taskin, A. A. & Ando, Y. Berry phase of nonideal Dirac fermions in topological insulators. *Phys. Rev. B* **84,** 035301 (2011).
36. Xiong, J. *et al*. High-field Shubnikov–de Haas oscillations in the topological insulator Bi_2Te_2Se. *Phys. Rev. B* **86,** 045314 (2012).
37. Ando, Y. Topological insulator materials. *J. Phys. Soc. Jpn* **82,** 102001 (2013).
38. Guo, Y. F. *et al*. Coupling of magnetic order to planar Bi electrons in the anisotropic Dirac metals $AMnBi_2$ (A = Sr, Ca). *Phys. Rev. B* **90,** 075120 (2014).
39. Wang, A. *et al*. Two-dimensional Dirac fermions in $YbMnBi_2$ antiferromagnet. *Phys. Rev. B* **94,** 165161 (2016).
40. Liu, J. Y. *et al*. Unusual interlayer quantum transport behavior caused by the zeroth Landau level in $YbMnBi_2$. Preprint at http://arxiv.org/abs/1608.05956 (2016).
41. Huang, S., Kim, J., Shelton, W. A., Plummer, E. W. & Jin, R. Nontrivial Berry phase in magnetic $BaMnSb_2$ semimetal. *Proc. Natl Acad. Sci. USA* **114,** 6256–6261 (2017).

Acknowledgements

The authors thank C. Wu at UCSD for helpful discussions. The work at Tulane University was supported by the NSF under Grant DMR-1205469 (support for personnel and materials) and Louisiana Board of Regents under grant LEQSF(2014-15)-ENH-TR-24 (support for equipment purchase). The neutron scattering work used resources at the High Flux Isotope Reactor, a DOE Office of Science User Facility operated by the Oak Ridge National Laboratory, and is supported by the US Department of Energy under EPSCoR Grant No. DE-SC0012432 with additional support from the Louisiana Board of Regents. The work at UNO is supported by the NSF under the NSF EPSCoR Cooperative Agreement No. EPS-1003897 with additional support from the Louisiana Board of Regents. The work at FSU and at the National High Magnetic Field Laboratory is supported by the NSF grant No. DMR-1206267, the NSF Cooperative Agreement No. DMR-1157490, and the State of Florida. Work at LANL was supported by the US DOE Basic Energy Science project 'Science at 100 Tesla'. The authors also acknowledge support from grant DOE DE-NA0001979.

Author contributions

J.Y.L., J.H. and Q.Z. equally contributed to this work. The single crystals used in this study were synthesized by J.Y.L. The magnetotransport measurements in 14 T PPMS were carried out by J.Y.L., D.J.A., Z.Q.M. and L.S. The high-field measurements at NHMFL were conducted by J.H., D.G., S.M.A.R., I.C., L.S. and Z.Q.M., G.F.C., X.L., J.W. and W.A.P. contributed to X-ray structure characterization and crystal quality examination. J.H., J.Y.L. and Y.L.Z. performed magnetization measurements. Q.Z., H.B.C., J.F.D. and D.A.T. conducted neutron scattering experiments and analyses. M.J. and F.B. did pulse magnetic field measurements. J.Y.L., J.H., Y.L.Z. and Z.Q.M. conducted transport data analyses. All authors contributed to scientific discussions and read and commented on the manuscript. This project was supervised by Z.Q.M.

Additional information

Supplementary information is available in the online version of the paper. Reprints and permissions information is available online at www.nature.com/reprints. Publisher's note: Springer Nature remains neutral with regard to jurisdictional claims in published maps and institutional affiliations. Correspondence and requests for materials should be addressed to Z.Q.M.

Competing financial interests

The authors declare no competing financial interests.

Methods

Single-crystal preparation. The $Sr_{1-y}Mn_{1-z}Sb_2$ (y or $z < 0.1$) single crystals were synthesized using a self-flux method with a stoichiometric mixture of Sr, Mn and Sb elements. The starting materials were put into a small alumina crucible and sealed in a quartz tube in an argon gas atmosphere. The tube was then heated to 1,050 °C for 2 days, followed by a subsequent cooling to 400 °C at a rate of $3\,^{\circ}\mathrm{C\,h^{-1}}$. Plate-like single crystals as large as a few millimetres were obtained (Fig. 1a, inset). The composition and structure of these single crystals was examined using energy-dispersive X-ray spectroscopy and X-ray diffraction measurements.

Magnetotransport and magnetization measurements. The magnetotransport measurements were performed with a four-probe method using 9 T/14 T Physics Property Measurement Systems and the 31 T resistive magnets at the National High Magnetic Field Laboratory (NHMFL) in Tallahassee. The magnetoresistivity measurements up to 65 T were performed using a four-probe method in a capacitor-bank-driven pulsed magnet at the NHMFL in Los Alamos. The experimental data collected under pulse fields and at constant temperatures between 0.6 K and 150 K were recorded on a digitizer using a custom-designed high-resolution low-noise synchronous lock-in technique running at 296 kHz. To minimize the eddy-current heating caused by the pulsed magnetic fields, a small crystal with dimensions of 0.8 mm × 0.7 mm × 0.4 mm was used for measurement. Magnetic fields were applied along the [100] axis. The a.c. currents used were between 1 and 10 mA, depending on the sample temperature. The magnetization measurements were carried out using a SQUID magnetometer (Quantum Design).

Berry phase determination by the fit of dHvA oscillation pattern to the LK formula. In addition to using the LL index fan diagram to determine the Berry phase ϕ_B, ϕ_B can also be obtained through the direct fit of the dHvA oscillation pattern to the multiband LK formula[42], in which the observed dHvA oscillations are treated as the linear superposition of two frequency (F'_α and F_β) oscillations. Each frequency oscillation can be described by the LK formula[43,44] that the takes Berry phase into account for a Dirac system[45]:

$$\Delta M \propto -B^{1/2} R_T R_D R_S \sin\left[2\pi\left(\frac{F}{B}-\gamma-\delta\right)\right]$$

where R_T is the temperature damping factor mentioned in the text, R_D $[=\exp(-\alpha T_D m^*/m_0 B)]$ and R_S $[=\cos(\pi g m^*/2m_0)]$ are Dingle and spin reduction factors respectively. T_D is the Dingle temperature. The thermal and Dingle damping are both due to LL broadening, whereas the spin reduction factor is associated with Zeeman splitting. The oscillation of ΔM is described by the sine term with a phase factor $-\gamma-\delta$, in which $\gamma=(1/2)-(\phi_B/2\pi)$. The phase shift δ, which is determined by the dimensionality of the Fermi surface, is 0 and $\pm1/8$, respectively for 2D and 3D cases. In our fit shown in Fig. 2d, δ is taken as zero, since the electronic band structure of $Sr_{1-y}Mn_{1-z}Sb_2$ is quasi-2D as discussed in the text. As shown in Fig. 2d, we fitted the dHvA oscillation pattern at 2 K to the LK formula with two frequency components. To reduce the number of fitting parameters, we took the values of m^*, F'_α and F_β obtained in Fig. 1f as fixed parameters.

To achieve the best fit, the FM background has to be precisely subtracted from the dHvA oscillation spectrum and this has to be done manually. Note that in the analyses of SdH oscillations, 'Igor' software was used to subtract the background and derive the FFT spectra (Fig. 1c). We also tried using 'Igor' to analyse the dHvA data and found that the background cannot be fully removed, so we chose to do manual background subtraction, which is quite successful as shown in Fig. 2e.

Neutron scattering measurements. Two relatively large $Sr_{1-y}Mn_{1-z}Sb_2$ (y and $z < 0.1$) crystals with masses of ~17 and 100 mg were investigated by neutron diffraction on a HB-3A four-circle diffractometer at the High Flux Isotope Reactor, Oak Ridge National Laboratory. One crystal was measured at 315 K above T_N with a wavelength of 1.003 Å from the bent Si-331 to study the crystal structure in the absence of $\lambda/2$ contamination[46], whereas the other crystal was measured with a wavelength of 1.542 Å that contains ~1.4% $\lambda/2$ contamination (Si-220 monochromator in high-resolution mode (bending 150))[46]. The crystal and magnetic structures were investigated at 5 K and the order parameter of nuclear/FM (200) and AFM (001) Bragg peaks was measured. Data were recorded over a temperature range of $5 < T < 760$ K using a closed-cycle refrigerator available at HB-3A. The SARAH representational analysis program[47] was used to derive the symmetry-allowed magnetic structures. All of the neutron diffraction data were analysed using the Rietveld refinement program FullProf suite[48].

Data availability. The authors declare that the main data supporting the findings of this study are available within this article and its Supplementary Information. Extra data are available from the corresponding author upon reasonable request. See author contributions for specific data sets.

References

42. Hu, J. *et al*. π Berry phase and Zeeman splitting of Weyl semimetal TaP. *Sci. Rep.* **6,** 18674 (2016).
43. Lifshitz, I. M. & Kosevich, A. M. Theory of magnetic susceptibility in metals at low temperatures. *Sov. Phys. JETP* **2,** 636–645 (1956).
44. Shoenberg, D. *Magnetic Oscillations in Metals* (Cambridge Univ. Press, 1984).
45. Mikitik, G. P. & Sharlai, Y. V. Manifestation of Berry's phase in metal physics. *Phys. Rev. Lett.* **82,** 2147–2150 (1999).
46. Chakoumakos, B. C. *et al*. Four-circle single-crystal neutron diffractometer at the High Flux Isotope Reactor. *J. Appl. Crystallogr.* **44,** 655–658 (2011).
47. Wills, A. S. A new protocol for the determination of magnetic structures using simulated annealing and representational analysis (SARAh). *Physica B* **276–278,** 680–681 (2000).
48. Rodríguez-Carvajal, J. Recent advances in magnetic structure determination by neutron powder diffraction. *Physica B* **192,** 55–69 (1993).